

## LETTERS

# Seismological constraints on a possible plume root at the core–mantle boundary

Sebastian Rost<sup>1</sup>, Edward J. Garnero<sup>1</sup>, Quentin Williams<sup>2</sup> & Michael Manga<sup>3</sup>

Recent seismological discoveries have indicated that the Earth's core–mantle boundary is far more complex than a simple boundary between the molten outer core and the silicate mantle. Instead, its structural complexities probably rival those of the Earth's crust<sup>1</sup>. Some regions of the lowermost mantle have been observed to have seismic wave speed reductions of at least 10 per cent<sup>2–7</sup>, which appear not to be global in extent<sup>7–9</sup>. Here we present robust evidence for an 8.5-km-thick and ~50-km-wide pocket of dense, partially molten material at the core–mantle boundary east of Australia. Array analyses of an anomalous precursor to the reflected seismic wave ScP reveal compressional and shear-wave velocity reductions of 8 and 25 per cent, respectively, and a 10 per cent increase in density of the partially molten aggregate. Seismological data are incompatible with a basal layer composed of pure melt, and thus require a mechanism to prevent downward percolation of dense melt within the layer. This may be possible by trapping of melt by cumulus crystal growth following melt drainage from an anomalously hot overlying region of the lowermost mantle. This magmatic evolution and the resulting cumulate structure seem to be associated with overlying thermal instabilities, and thus may mark a root zone of an upwelling plume.

Partial melting of lowermost mantle rock<sup>10,11</sup> and chemical reactions between mantle and core material<sup>12–14</sup> are viable candidates for causing ultralow velocity zone (ULVZ) structure at Earth's core–mantle boundary (CMB); each has distinct effects on seismic properties. Determining the likely cause(s) for ULVZ hinges on constraining ULVZ spatial extent, density and seismic velocity<sup>10,14,15</sup>, and the sharpness of the boundary between ULVZ and overlying mantle. We investigate the CMB east of Australia, slightly south of New Caledonia, where P- and S-wave velocity ( $v_P$  and  $v_S$ , respectively) reductions are seen in the lower mantle<sup>16,17</sup>, and complex CMB properties have been detected in isolated locations<sup>5,7,18</sup>. In this study, an unprecedented high-resolution CMB sampling over a  $100 \times 250$  km region is achieved using a newly assembled data set of 305 Tonga–Fiji earthquakes recorded at the small aperture (20 km) Warramunga seismic array (WRA), equipped with 20 short-period (~1 Hz dominant period) vertical-component seismometers (Fig. 1a). This level of spatial sampling distinguishes our study from previous, broader wavelength ULVZ investigations. Earthquakes were chosen on the basis of simple and similar source-time functions, and deep focal depths (>450 km) to minimize upper mantle attenuation and scattering effects and to avoid surface reflected phases. Data displaying complex source-time functions, clipping, or low signal-to-noise ratio (SNR) were omitted.

The seismic wave ScP travels from earthquake to CMB as an S wave, converts to a P wave upon reflection, and returns to the surface as a P wave. ScP waveforms from each event were beam-formed, a method that stacks data in the direction that maximizes ScP

coherency and amplitude, and significantly increases the SNR while minimizing possible influence of crustal structure beneath array stations. Figure 1b shows ScP stacks for the most densely sampled CMB region in our study area. Records between  $-24.60^\circ$  and  $-25.10^\circ$  in latitude show a very coherent precursor ~1.8 s before ScP. Separately summing the simple and anomalous records highlights the precursor existence (Fig. 1c). Precursor evidence vanishes less than ~20 km from the central anomalous zone; several records sampling this transition exhibit complex behaviour, suggesting multipathing.

Interaction of ScP with the top of a ULVZ generates a precursor<sup>4,5,19</sup> by reflection (and conversion) from S-to-P at the top of the ULVZ, as well as an S-to-P conversion at the ULVZ surface, which continues downward as a P wave. ULVZ structure can also generate later arriving phases that are more difficult to detect and analyse, as they arrive in the ScP coda. In our data set, the dominant precursory energy is a conversion at the top of the ULVZ instead of the CMB, thus arriving sooner. A very compact region of the study area roughly 50 km in dimension is dominated by clustering of the highest quality ULVZ precursors (Fig. 2). This small dimension with well resolved sharp edges is significantly smaller than that resolvable in previous studies<sup>6,7</sup>.

ScP precursor timing, amplitude and waveform were modelled with gaussian beam<sup>20</sup> synthetic seismograms (Fig. 3a). All dominant ULVZ P or S reflections, reverberations and conversions were included in the modelling, as well as a source mechanism that fits observed P waveforms. We explored a wide parameter space (Fig. 3), and constrain best-fit model properties:  $8.5 \pm 1$  km thick,  $8 \pm 2.5\%$   $v_P$  and  $25 \pm 4\%$   $v_S$  reductions, and  $10 \pm 5\%$  density increase (Fig. 3b). Models lacking a density increase poorly fit the observed waveforms; as seen in Fig. 3, ScP precursory energy is very sensitive to ULVZ density, in fact tolerating only slight offsets ( $\leq 2\%$ ) from the best fit 10% value before waveform degradations occur. The geometric and elastic uncertainties are substantially less than those of previous ULVZ studies<sup>3,7,21</sup>. We note that our finding of a 10% density anomaly is considerably less than the 18–33% that have been found for ULVZ generated by iron-rich subducted sediments<sup>22</sup>.  $D''$  anisotropy (for example, due to the post-perovskite phase<sup>15</sup>) may split the S part of ScP. But to yield ScP with a precursor, two pulses with SV energy are required; furthermore, the anisotropic zone needs to be several hundred kilometres thick (to match the 1.8 s precursor time) and limited to a narrow corridor around the paths displaying precursors. Both of these requirements are less likely than the simpler ULVZ structure we propose here.

A diagram of the best-fitting ULVZ structure is shown in Fig. 4. The elevated density reflects the aggregate density of the liquid and solid of the partially molten assemblage: the relative density contrast between liquid and solid is unclear. Our modelling is principally

<sup>1</sup>Department of Geological Sciences, Arizona State University, Box 871404, Tempe, Arizona 85287-1404, USA. <sup>2</sup>Department of Earth Sciences, University of California Santa Cruz, 1156 High Street, Santa Cruz, California 95064, USA. <sup>3</sup>Department of Earth and Planetary Science, University of California Berkeley, 307 McCone Hall, Berkeley, California 94720-4767, USA.

sensitive to average ULVZ properties; the internal zonation is not resolved. However, the upper ULVZ boundary is seismically sharp, with a probable width of less than  $\sim 1$  km: the rapid onset is consistent with most (if not all) of the velocity decrement occurring near the ULVZ surface.

We performed slowness-backazimuth stacks, and rule out strong reflections from off-great-circle paths as a source of the precursors. We also rule out multipathing or scattering in the source region, as earthquakes that produce the ScP precursors are distributed over a 170 km depth range, and over a 90 km linear section of the Fiji-Tonga trench; a strong scatterer would be required roughly 20 km from each source over this dimension, which should produce more precursor travel time variation. Neighbouring sources should detect it as well, from a variety of distances.

Our best-fit  $v_S$ -to- $v_P$  reduction of 25:8 is very close to the expected 3:1 for partial melt<sup>10,14</sup>; an 8%  $v_P$  decrease can be explained by a 5–30% volume fraction of melt, depending on the melt geometry<sup>10</sup>. Partial melting is therefore a strong candidate for explaining our observations, and consistent with higher than average temperatures producing observed low (tomographically derived) seismic velocities in this region. A fully molten layer produces waveforms incompatible with observations. The presumably low-viscosity, dense, partially molten material clearly has not spread out along the CMB; neither

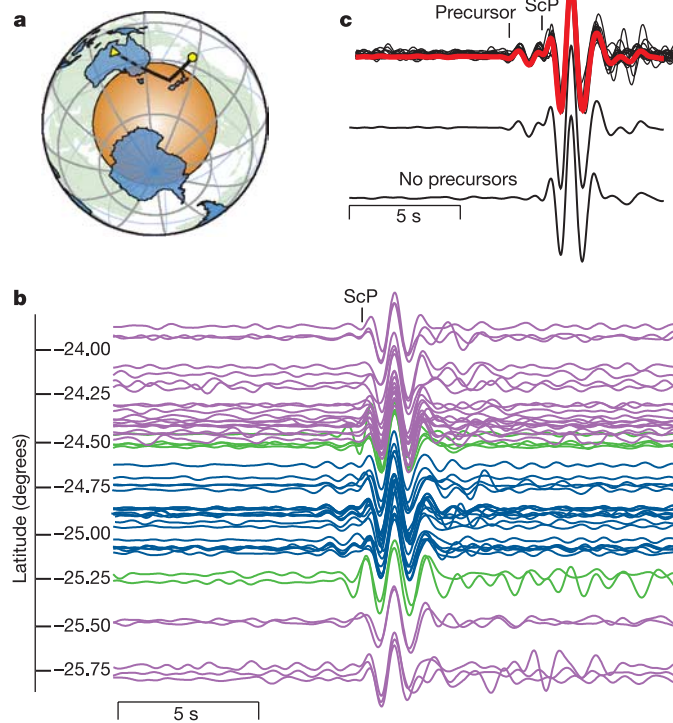


**Figure 1 | Array beams of ScP and precursors.** **a**, Source-receiver combination from earthquakes in the Tonga-Fiji region (circle) to the Warramunga array (triangle). **b**, Array beam traces of the original short-period array recordings aligned on the ScP arrival sorted with respect to the latitude of the ScP CMB reflection point, from  $-23.8^\circ$  to  $-25.75^\circ$  in a north-south profile. The epicentral distance range spanned by these data are  $40.8^\circ$  to  $46.8^\circ$ . The longitudinal extension of the sources is only a few degrees owing to the configuration of sources in the Tonga-Fiji subduction zone. The processing of the data are restricted to filtering with a second order bandpass with cut-off frequencies of 0.5 Hz and 1.4 Hz. Blue traces show a precursor arriving 1.8 s before ScP. Green traces show complicated waveforms with evidence of anomalous multipathing. Purple traces show no waveform complications. **c**, Precursory traces (blue signals in **b**) in comparison to events lacking the precursor (purple signals in **b**). Also shown are the summation traces for the precursor and non-precursor waveforms.

has the liquid (certainly denser than the overlying mantle material) drained downwards and segregated from its neighbouring solids.

The notable increase in density of the region implies that a simple elevation of isotherms<sup>7,21</sup> is unlikely to explain fully the presence of this ULVZ micro-patch: a coupled dynamical and chemical, rather than solely thermal, explanation is required. The sharpness and high melt fraction are not consistent with simple compaction of a partially molten zone<sup>23</sup>—and dense melt produced in an upwelling will drain downward, drainage will be most effective where the porosity (and hence permeability) is high, and a diffuse low-melt-fraction region should thus persist on the top of the layer.

One key seismological inference is the apparently uniform ULVZ property of proximity to the critical percolation threshold of liquid, if liquid is present in isolated and randomly-positioned pockets<sup>24</sup>. Indeed, a principal enigma of ULVZ models is that partial melt exists without apparent segregation over broad regions of the CMB. High matrix permeability from interconnected melt requires no density difference between coexisting liquid and solids in order to maintain partial melt throughout the ULVZ (an unlikely but not impossible situation<sup>25</sup>). This is not consistent with the seismic modelling.

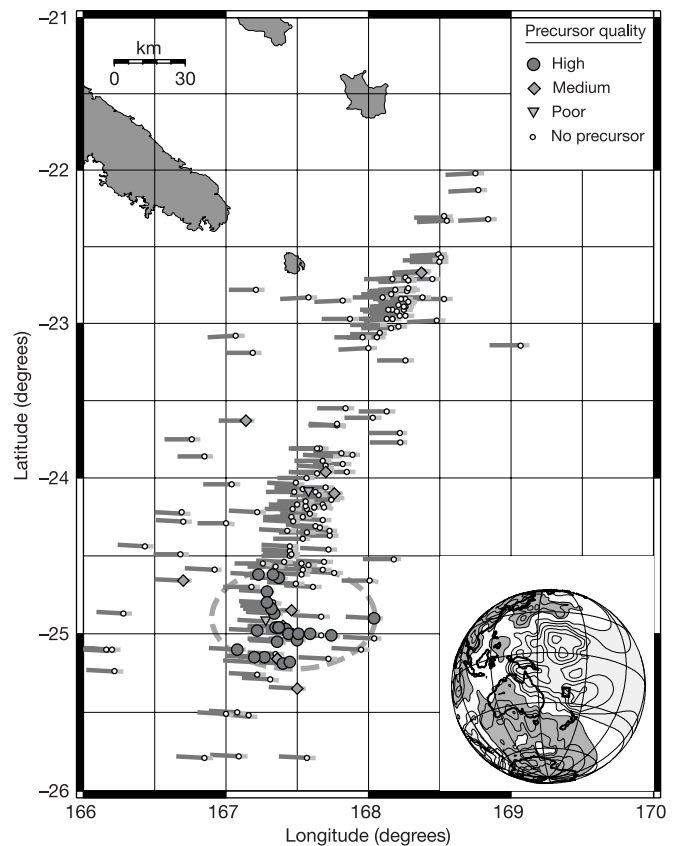


**Figure 2 | ULVZ detections at ScP core-reflection locations.** Clear non-detections of precursory energy to ScP are marked with small open circles. Short grey horizontal line segments denote the S- and P-wave segments (to the right and left of symbols, respectively) of ScP in an 8-km-thick ULVZ. Precursor quality is also noted, which is a measure of the precursor amplitude compared to background signal-to-noise ratio. The dashed grey line shows the region with the coherent precursor shown in Fig. 1. Inset globe displays the tomographically derived shear-wave heterogeneity<sup>20</sup> for the lowermost 200 km of the mantle, upon which the region of the larger map is denoted (small rectangle towards centre of globe). Lighter and darker shading corresponds to lower and higher relative wave speeds, respectively. Contour lines are in 0.5% intervals, and the interval  $-0.5\% < v_S < +0.5\%$  is not shaded. Our study region coincides with a very-low-velocity region.

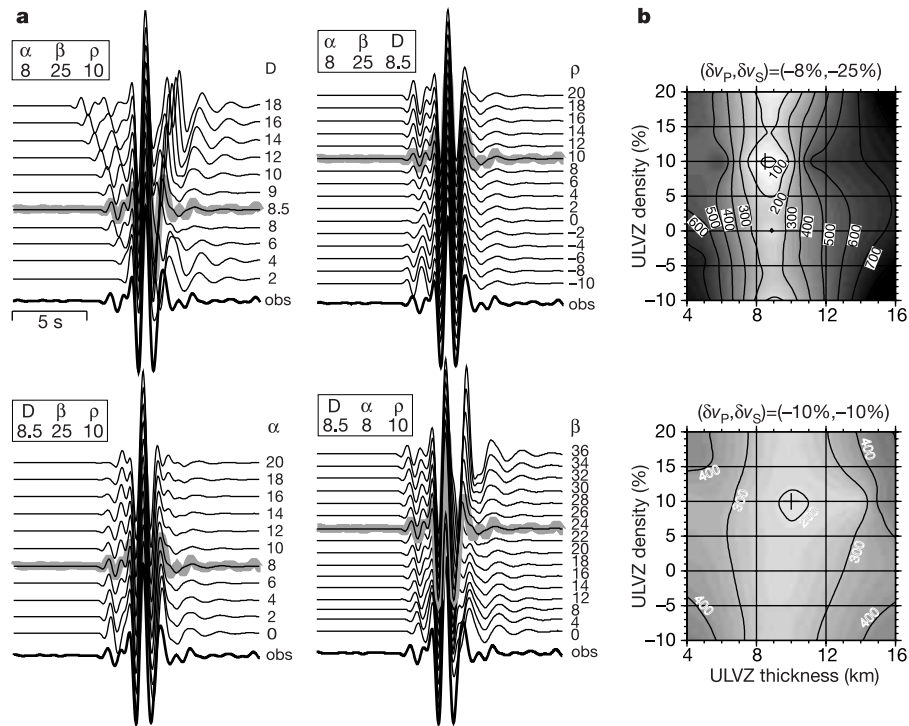


**Figure 3 | Synthetic waveform modelling of ScP precursors.** **a**, Synthetic seismograms for varying ULVZ thickness,  $v_p/v_s$  and density. For comparison, the ScP precursor data trace is shown at the bottom of each panel and as a light grey line beneath the best-fitting model of each model class. The best-fit model has an 8.5-km-thick ULVZ with P and S reductions of 8% and 25%, respectively, and a 10% density increase. Models with differing thickness ('D'), P and S velocity decreases ( $\alpha$ ' and  $\beta$ '), respectively), and density increases ( $\rho$ ') are shown. We note that a strong density increase is necessary to fit the observed waveforms. Additional waveform modelling is presented in Supplementary Information. **b**, Goodness of fit of

synthetic predictions to data. The quality of fit is calculated by computing a residual trace by subtracting synthetic waveforms from the data in a 10 s time window around the ScP arrival, taking the envelope of the residual trace, and integrating (thus, a proxy for residual energy representing misfit). Two fixed  $v_p/v_s$  ratios (8:25 and 10:10) are shown for varying ULVZ thickness and density. Models with  $v_p/v_s$  of 1:1 show a worse fit to the data: the minimum misfit energy in the 8:25 plot is 15, compared to 188 for the 10:10 case. The detection level threshold for ULVZ thickness in this study is  $\sim 4$  km.

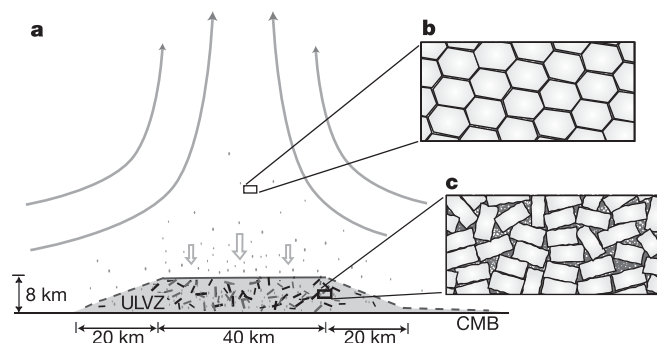


**Figure 4 | Preferred model of dense partially molten ULVZ.** **a**, ULVZ structural parameters of best-fitting model, in a south to north cross-section corresponding to dashed region in Fig. 2. Dense melt from above percolates downward (**b**); whether this melt chemically re-equilibrates with its neighbouring solids while descending is unknown. Melt accumulates within the ULVZ (**c**), where it is sequestered as an intercumulus liquid at concentrations just below the percolation threshold. Both intercumulus crystal growth and compaction effects are probably critical in determining the properties of this zone. The precise crystal dimensions (black dashes in ULVZ region) are uncertain, but coarsening of crystals via intercumulus growth could markedly enhance crystal sizes within the ULVZ relative to those within the overlying mantle. The amount of melt in the mantle region above the CMB probably does not exceed 0.2%, based on the size of observed seismic velocity decrements, while that within the ULVZ is near 25%.

Alternatively, melt may be trapped within the ULVZ as an intercumulus liquid: crystals within an initially partial molten system are progressively overgrown, trapping residual (and incompatible-element enriched) liquid. The elevated density may be associated with iron partitioning into the silicate liquid, and resultant enrichment of the ULVZ in iron<sup>26</sup>; progressive cumulate growth is likely to generate iron-rich crystals coexisting with these liquids. The wetting behaviour (and chemistry) of such melts is ill-constrained. However, dense melts that readily form interconnected networks are likely to descend to the core: therefore, the ULVZ may only retain liquids whose wetting behaviour allows them to be trapped. The genesis of a cumulate layer is probably related to downward melt percolation and intercumulus crystal growth as melt interacts with lowermost mantle solids, compatible with the seismic observations.

The geodynamic implications of such partial melting and cumulate formation are profound; large overlying thermal anomalies are required, which in turn are probably connected to dynamic instabilities that give rise to mantle plumes. This is consistent with the general correlation between ULVZ locations, reduced lowermost mantle velocities<sup>7,27</sup>, and hotspot volcanism<sup>27</sup>. Furthermore, if the lowermost mantle is adiabatic and the slope of the mantle solidus is positive and larger than the adiabat, such cumulus growth and melt trapping should occur as melts partially resolidify on descent<sup>28</sup>. Thus, the solid matrix of the ULVZ may contain relatively large, annealed crystals whose chemistry is modulated by precipitation of the coexisting liquid, juxtaposed with pockets of strongly incompatible element enriched melt trapped in intercumulus regions. It is possible that continual or episodic recharge (and possible discharge into the

core) of melt keeps the system near the critical percolation threshold for melt.

The seismically determined ULVZ dimensions, coupled with the well-constrained large density contrast, provide constraints on lower mantle dynamics and properties. For example, if we assume that the shape of the partial melt pocket is approximately steady over geological timescales, and that ULVZ patches form below upwellings (Fig. 4), then ULVZ thickness and radial extent can be estimated by balancing viscous stresses caused by the upwelling flow in the surrounding mantle with buoyancy forces that will cause the layer to spread (see Supplementary Information). A density difference of 10%, a thickness of 8 km and radial extent of 25 km, and a viscosity of  $10^{19}$  Pa s imply a reasonable upwelling velocity of  $0.1 \text{ m yr}^{-1}$ .

The existence of melt in this very-low-seismic-velocity, and presumably hot, region of  $D''$  is not unexpected. Tomographic images do not have sufficient resolution to image small-scale plume-like features, but in a recent study<sup>29</sup> broader scale (greater than  $\sim 200$  km) plume features have been imaged, and low velocities in our study region are suggested. Geodynamic modelling of mantle flow based on tomographic models<sup>30</sup> indicates that the roots of three plumes (Tasmanid, Lord Howe and East Australia) are in the vicinity of our study area, but the CMB-to-surface extension of these features remains unclear.

The processes of melt segregation and drainage from above, coupled with chemical modification of the liquid by postcumulus crystal growth and/or interaction with the core, will each serve to generate a liquid enriched in incompatible elements. Therefore, if heat-producing elements continue to be partitioned into silicate liquid at CMB conditions, we expect this type of zone to not only be initially generated by melt drainage from a hot thermal upwelling, but also to function as a long-lived root for upwellings<sup>31</sup>. As a result, such localized patches of dense ULVZ melt may produce a fixed base for hot upwellings, and thus plumes: indeed, the genesis and longevity of whole mantle plumes may be intimately tied to the production of a ULVZ at their base.

Received 2 February; accepted 6 April 2005.

- Garnero, E. J. Heterogeneity of the lowermost mantle. *Annu. Rev. Earth Planet. Sci.* **28**, 509–537 (2000).
- Mori, J. & Helmlinger, D. V. Localized boundary layer below the mid-Pacific velocity anomaly from a PcP precursor. *J. Geophys. Res.* **100**, 20359–20365 (1995).
- Garnero, E. J. & Helmlinger, D. V. Further structural constraints and uncertainties of a thin laterally varying ultralow-velocity layer at the base of the mantle. *J. Geophys. Res.* **103**, 12495–12509 (1998).
- Reasoner, C. & Revenaugh, J. ScP constraints on ultralow-velocity zone density and gradient thickness beneath the Pacific. *J. Geophys. Res.* **105**, 28173–28182 (2000).
- Rost, S. & Revenaugh, J. Small-scale ultralow-velocity zone structure imaged by ScP. *J. Geophys. Res.* **108**(B1), 2056, doi:10.1029/2001JB001627 (2003).
- Rondenay, S. & Fischer, K. M. Constraints on localized core-mantle boundary structure from multichannel, broadband SKS coda analysis. *J. Geophys. Res.* **108**(B11), 2537, doi:10.1029/2003JB002518 (2003).
- Thorne, M. & Garnero, E. J. Inferences on ultralow-velocity zone structure from a global analysis of SPdKS waves. *J. Geophys. Res.* **109**, B08301, doi:10.1029/2004JB003010 (2004).
- Castle, J. C. & Van der Hilst, R. D. The core-mantle boundary under the Gulf of Alaska: No ULVZ for shear waves. *Earth Planet. Sci. Lett.* **176**, 311–321 (2000).
- Persh, S. E. & Vidale, J. E. Reflection properties of the core-mantle boundary from global stacks of PcP and ScP. *J. Geophys. Res.* **109**, B04309, doi:10.1029/2003JB002768 (2004).
- Williams, Q. & Garnero, E. J. Seismic evidence for partial melt at the base of Earth's mantle. *Science* **273**, 1528–1530 (1996).
- Vidale, J. E. & Hedlin, M. A. H. Evidence for partial melt at the core-mantle boundary north of Tonga from the strong scattering of seismic waves. *Nature* **391**, 682–685 (1998).
- Knittle, E. & Jeanloz, R. Earth's core-mantle boundary; results of experiments at high pressures and temperatures. *Science* **251**, 1438–1443 (1991).
- Song, X. & Ahrens, T. J. Pressure-temperature range of reactions between liquid iron in the outer core and mantle silicates. *Geophys. Res. Lett.* **21**, 153–156 (1994).
- Berryman, J. G. Seismic velocity decrement ratios for regions of partial melt in the lower mantle. *Geophys. Res. Lett.* **27**, 421–424 (2000).
- Murakami, M., Hirose, K., Kawamura, K., Sata, N. & Ohishi, Y. Post-perovskite phase transition in  $\text{MgSiO}_3$ . *Science* **304**, 855–858 (2004).
- Karason, H. & van der Hilst, R. D. Tomographic imaging of the lowermost mantle with differential times of refracted and diffracted core phases (PKP,  $P_{\text{diff}}$ ). *J. Geophys. Res.* **106**, 6569–6587 (2001).
- Grand, S. P. Mantle shear-wave tomography and the fate of subducted slabs. *Phil. Trans. R. Soc. Lond. A* **360**, 2475–2491 (2002).
- Rost, S. & Revenaugh, J. Seismic detection of rigid zones at the top of the core. *Science* **294**, 1911–1914 (2001).
- Garnero, E. J. & Vidale, J. E. ScP; a probe of ultralow velocity zones at the base of the mantle. *Geophys. Res. Lett.* **26**, 377–380 (1999).
- Cerveny, V. & Psencik, I. Gaussian beams in elastic 2-D laterally varying layered structures. *Geophys. J. Int.* **78**, 65–91 (1984).
- Garnero, E. J., Revenaugh, J., Williams, Q., Lay, T. & Kellogg, L. H. in *The Core-Mantle Boundary Region* (eds Gurnis, M., Wysession, M., Knittle, E. & Buffett, B.) 319–334 (Geodynamics series, Vol. 28, American Geophysical Union, Washington DC, 1998).
- Dobson, D. P. & Brodholt, J. P. Subducted iron formations as a source of ultralow-velocity zones at the core-mantle boundary. *Nature* **434**, 371–374 (2005).
- McKenzie, D. P. The extraction of magma from the crust and mantle. *Earth Planet. Sci. Lett.* **74**, 81–91 (1985).
- Roscoe, R. The viscosity of suspensions of rigid spheres. *J. Appl. Phys.* **3**, 267–269 (1952).
- Akins, J. A., Luo, S.-N., Asimow, P. D. & Ahrens, T. J. Shock-induced melting of  $\text{MgSiO}_3$  perovskite and implications for melts in Earth's lowermost mantle. *Geophys. Res. Lett.* **31**(14), doi:10.1029/2004GL020237 (2004).
- Knittle, E. in *The Core-Mantle Boundary Region* (eds Gurnis, M., Wysession, M., Knittle, E. & Buffett, B.) 119–130 (Geodynamics Series, Vol. 28, American Geophysical Union, Washington DC, 1998).
- Williams, Q., Revenaugh, J. & Garnero, E. J. A correlation between ultralow basal velocities in the mantle and hot spots. *Science* **281**, 546–549 (1998).
- Walker, D., Agee, C. & Zhang, Y. Fusion curve slope and crystal/liquid buoyancy. *J. Geophys. Res.* **93**, 313–323 (1988).
- Montelli, R. et al. Finite-frequency tomography reveals a variety of plumes in the mantle. *Science* **303**, 338–343 (2004).
- Steinberger, B. Plumes in a convecting mantle: Models and observations for individual hotspots. *J. Geophys. Res.* **105**, 11127–11152 (2000).
- Jellinek, A. M. & Manga, M. The influence of a chemical boundary layer on the fixity, spacing and lifetime of mantle plumes. *Nature* **418**, 760–763 (2002).

Supplementary Information is linked to the online version of the paper at [www.nature.com/nature](http://www.nature.com/nature).

**Acknowledgements** We thank R. van der Hilst and S. Grand for supplying tomographic models, S. Grand for a Futterman  $t^*$  code, and the Seismological group of MoD at Blacknest for the WRA data set. This research was supported by NSF.

**Author Information** Reprints and permissions information is available at [ngp.nature.com/reprintsandpermissions](http://ngp.nature.com/reprintsandpermissions). The authors declare no competing financial interests. Correspondence and requests for materials should be addressed to S.R. (srost@asu.edu).